NANO LETTERS

Letter

pubs.acs.org/NanoLett

Detecting 20 nm Wide Defects in Large Area Nanopatterns Using Optical Interferometric Microscopy

Renjie Zhou,[†] Chris Edwards,[†] Amir Arbabi,[†] Gabriel Popescu,[‡] and Lynford L. Goddard*[,†]

[†]Micro and Nanotechnology Laboratory, Department of Electrical and Computer Engineering, University of Illinois at Urbana−Champaign, Urbana, Illinois 61801, United States

[‡]Quantitative Light Imaging Laboratory, Department of Electrical and Computer Engineering, Beckman Institute for Advanced Science and Technology, University of Illinois at Urbana−Champaign, Urbana, Illinois 61801, United States

Supporting Information

ABSTRACT: Due to the diffraction limited resolution and the presence of speckle noise, visible laser light is generally thought to be impractical for finding deep subwavelength defects in patterned semiconductor wafers. Here, we report on a nondestructive low-noise interferometric imaging method capable of detecting nanoscale defects within a wide field of view using visible light. The method uses a common-path laser interferometer and a combination of digital image processing techniques to produce 70 μm by 27 μm panoramic phase and amplitude images of the test nanopattern. Significant noise reduction and high sensitivity are achieved, which enables successful detection of several different types of sparse defects with sizes on the order of 20 nm wide by 100 nm long by 110 nm tall.

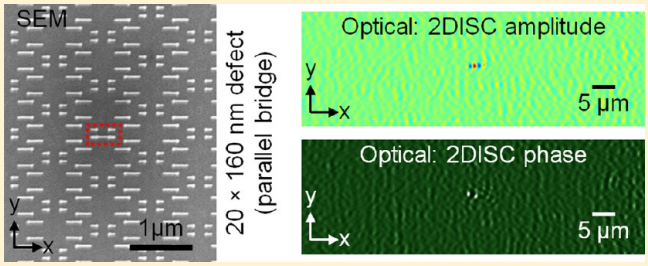

KEYWORDS: *Interferometric optical microscopy, defect inspection, metrology, phase measurement, nanotechnology*

An isolated defect buried in a nanopattern can substantially affect the functionality of the whole device.[1−3] Thus, detecting defects during nanofabrication is critical for maintaining a high yield.[4−6] Scanning electron microscopy (SEM) and atomic force microscopy (AFM) are typically used for nanopattern inspection.[7−9] However, SEM has low throughput and can be destructive,[10−12] and AFM typically has extremely low throughput.[13−15] These characteristics make them unsuitable for in-line defect inspection. Optical microscopy is usually nondestructive and has high throughput due to its relatively large field of view (FOV), but its resolution is diffraction limited to approximately $\lambda/2$.[16] To detect deep subwavelength defects, one approach has been focused on improving the resolution, such as developing ultraviolet and high-order harmonic laser sources,[17−21] or very high numerical aperture lenses.[22−26] These methods typically have a small FOV because of the available cameras at these wavelengths, and can still potentially damage a wafer during fabrication due to the short wavelength, high pulse energy,[27−30] and physical contact with the wafer.

The ultimate limiting factor for defect detection is not resolution, but rather noise.[31−34] Noise decreases image contrast and reduces sensitivity. Thus, we have developed a new low-noise optical microscope imaging system with high sensitivity to overcome these issues. This system uses a highly sensitive common-path interferometer and image postprocessing techniques targeted to mitigate the effects of characteristic noise sources. With these improvements, we successfully detected subwavelength defects in large area patterns with visible light interferometric imaging.

Optical interferometry can provide nanoscale information because it provides access to phase.[35] Quantitative phase imaging has become an emerging field for biomedical applications.[36] Diffraction phase microscopy (DPM) uses a common-path interferometer to measure both the reflection amplitude and phase from a sample.[37] The common-path geometry makes it less sensitive to vibrational noise compared with conventional dual-path interferometers. Transmission DPM and epi-illumination (reflection) DPM (epi-DPM) have previously demonstrated sensitivity to nanometer changes in height.[37−39] For defect detection, we built a specialized epi-DPM system. In a single epi-DPM image, defect visibility is extremely poor due to the deep subwavelength defect size and the residual noise in the image. Thus, we developed a comprehensive image postprocessing method to digitally remove different types of noise based on their properties. The method includes second order difference, image stitching, and convolution (2DISC). The postprocessing technique uses a sequence of images obtained by translating the wafer parallel to its surface and then performs the second order difference operation to reduce spatial noise, stitches the result together to form a panoramic image to reduce temporal noise, and finally convolves the result with a matched pattern to boost the signal-

Received: May 3, 2013
Revised: July 9, 2013
Published: July 30, 2013

   dx.doi.org/10.1021/nl401622b | *Nano Lett.* 2013, 13, 3716−3721

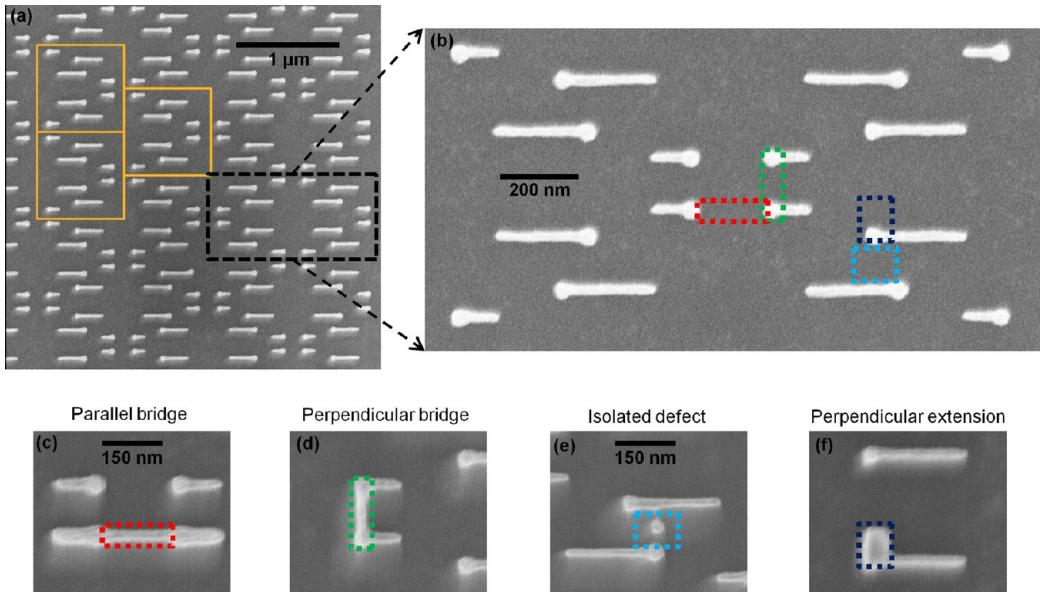

Figure 1. SEM images illustrate the printed defects in the large area nanopatterned structure. (a) A defect free portion of the pattern, showing the unit cell in orange. (b) A zoomed-in portion of the pattern, where the locations of the four different type of defects are marked by colored boxes. (c) A parallel bridge defect (red). (d) A perpendicular bridge defect (green). (e) An isolated dot defect (light-blue). (f) A perpendicular line extension defect (dark-blue).

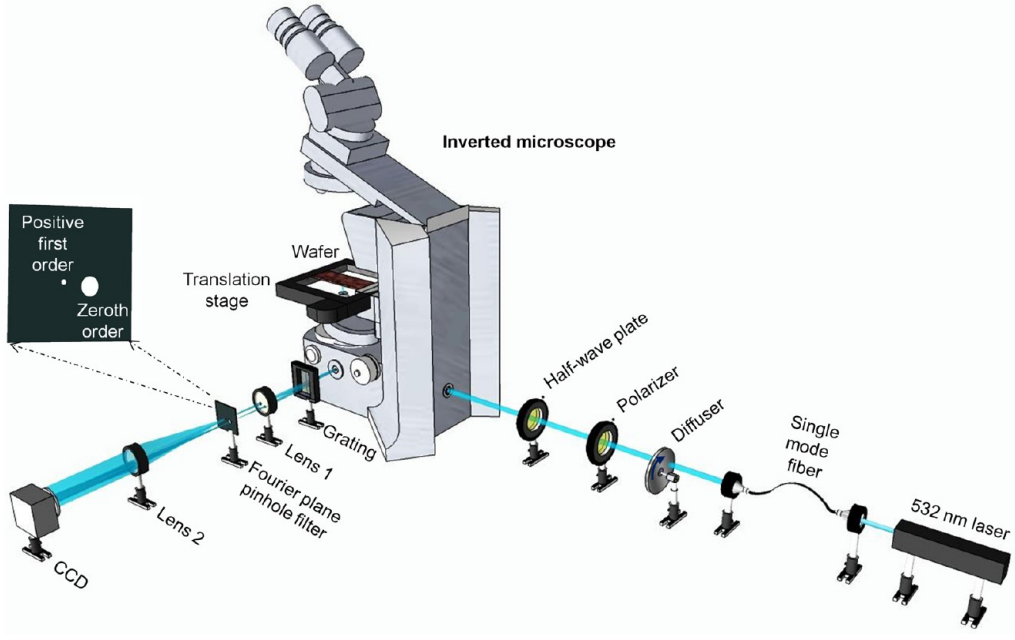

Figure 2. Epi-DPM system configuration. This system uses a common-path interferometer geometry. The pinhole filter is used for filtering one copy of the beam after the grating into a reference beam. The signal beam and reference beam interfere at the CCD camera to form the interferogram.

to-noise ratio (SNR) from the defect. The defect detectability of the 2DISC method is studied using receiver operating characteristic (ROC) curves. Using 2DISC, we consistently detected various types of defects with sizes down to 20 nm wide by 100 nm long by 110 tall in a 70 μm by 27 μm panoramic image and then verified their locations and shapes using SEM. Since the defect height is the same for all samples, we will just use the transverse dimensions to describe the defect size.

A defect free portion of the wafer is shown in Figure 1a. This pattern is periodic and consists of parallel lines made of polysilicon on a silicon substrate. The pattern consists of two different lines that are 22 nm in width, 120 or 260 nm in length, and 110 nm in height. The lines are arranged to form a 0.8 μm by 0.8 μm square unit cell containing 8 lines. The unit cell is repeated in a rhombic lattice pattern to form a 2-dimensional array with an area of 100 μm by 100 μm. Figure 1b shows a zoomed-in portion of the defect free pattern with the locations of four different types of defects indicated. Parallel (red) and perpendicular (green) bridge defects are shown in Figure 1, parts c and d, respectively; an isolated (light blue) defect is shown in Figure 1e, and a line extension (dark blue) defect is shown in Figure 1f. Each defect is located in the center of the 2-dimensional array and only one defect type is printed per array.

dx.doi.org/10.1021/nl401622b | *Nano Lett.* 2013, 13, 3716−3721

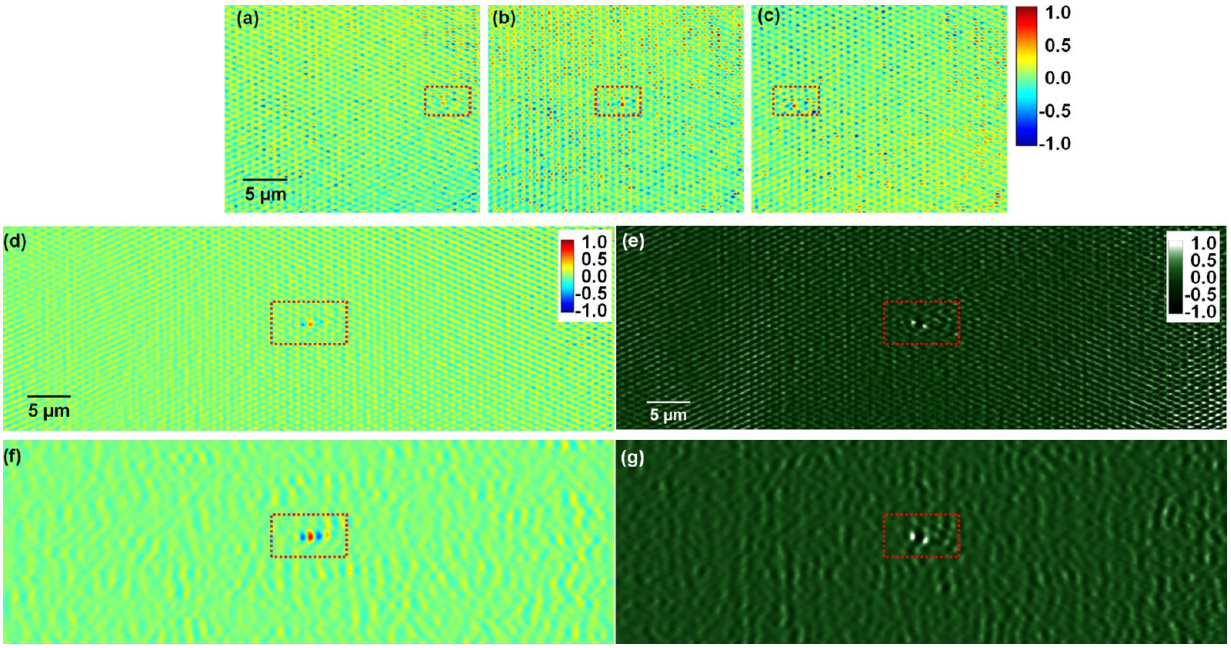

Figure 3. Illustration of the 2DISC method for defect detection. A defect array with a 20 nm by 160 nm parallel bridge defect in the center is used as an example. (a–c) Example of second order difference amplitude image frames showing the defect moving right to left across the field of view as the wafer is translated to the left. (d, e) Panoramic second order difference amplitude and phase images, respectively. These are the 2DISC images prior to the convolution step. (f, g) Full 2DISC amplitude and phase images, respectively. For each image, the location of the defect is marked by a red rectangular box.

In adjacent arrays, various sizes of these defects are printed by varying the line width of the defect. In the following sections, we will introduce the defect inspection system and image postprocessing method for finding the defects.

The epi-DPM system is illustrated in Figure 2. The system uses a 532 nm frequency-doubled Nd:YAG laser as the illumination source. The laser is first coupled into a single-mode fiber for filtering out the high order transverse modes. After the fiber, the beam is collimated and passes through a rotating diffuser to reduce the laser speckle noise. Then, the laser goes through a linear polarizer and half-wave plate, which are used to control the angle of the laser polarization relative to the wafer structure. After that, the beam enters an inverted microscope and is normally incident on the wafer. The reflected beam exits the microscope and is incident on a blazed diffraction grating (300 lines per mm) where multiple orders of the beam are created. We select two orders, specifically the positive first order and the zeroth order, to pass through a 4-f system which has a 75 mm focal length first lens and a 400 mm focal length second lens. The positive first order beam has the highest diffraction intensity and is low-pass filtered through a 10 μm pinhole to serve as the reference beam, and the zeroth order beam serves as the signal beam. The two beams interfere at the CCD camera plane where the interferograms are captured. The common-path geometry and the rotating diffuser are used to physically reduce the noise.[39] From the interferogram, the reflected wave amplitude and phase are retrieved[39,40] (see Supporting Information). The phase image contains information about the sample's topography and the amplitude image quantifies the variation in the sample's reflection coefficient.

The microscope uses a 40× objective with a numerical aperture (NA) of 0.9 (EC Plan-Neofluar 40×/0.9 Pol) and has a FOV of 30 μm by 27 μm. According to the Rayleigh criterion, the diffraction limited resolution is calculated to be about $1.22\lambda/(\mathrm{NA}_{\mathrm{objective}} + \mathrm{NA}_{\mathrm{condenser}}) = 720$ nm since $\mathrm{NA}_{\mathrm{condenser}} = 0$ for collimated illumination. Thus, individual features of the patterned wafer will not be resolvable, but rather blurred by the point spread function (PSF) of the system. Since the features under inspection are deep subwavelength, the system is still far from detecting defects in the pattern. Any subtle residual noise present in the system can greatly affect the image contrast. Also, slight system calibration errors such as defocus, sample-tilt, aberration, nonuniformity or time-varying illumination intensity can also degrade the image quality substantially. An example of a recorded interferogram of the patterned wafer and its retrieved phase and amplitude images are shown in the Supporting Information to show that it is impossible to discern the defect signal from a single image. In order to detect the defect, we collect a sequence of images by translating the wafer in the direction parallel to the underlying line structure. With the scanning images, we can remove different types of noise and system imperfections and then extract the defect signal.

Here, we explain the 2DISC method for removing noise and system imperfection. We define system imperfection as the noise in the image profile due to nonuniformity in the illumination source, illumination path, or camera response. We will illustrate the 2DISC method using the array region that has a 20 nm by 160 nm size parallel bridge defect (Figure 1c). First, a sequence of 90 interferogram frames with adjacent frame horizontal translation steps of 0.75 μm is collected. The choice of translation direction and step size are explained in the Supporting Information. We calculate the amplitude and phase for each image from the captured interferograms. As described previously, in a single amplitude or phase image, we cannot detect the defect due to the different types of residual noise. The spatial distribution of noise can be decomposed into time-variant and time-invariant sources. Time invariant noise is mostly due to the laser speckles created at the optical component surfaces. Since this noise is also shift-invariant,

dx.doi.org/10.1021/nl401622b | *Nano Lett.* 2013, 13, 3716–3721

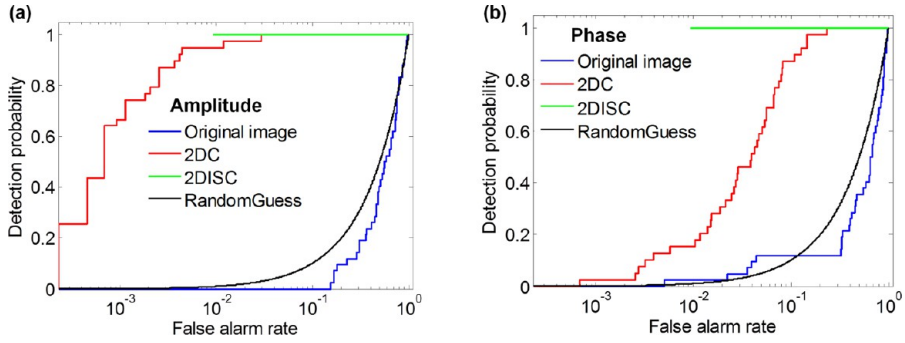

Figure 4. Study of defect detectability with the 2DISC method using ROC curves. (a) The blue, red, green, and black curves are for the original amplitude single images, the second order difference with convolution (2DC), the full 2DISC panoramic image, and random guessing, respectively. (b) Corresponding ROC curves for the phase images. From parts a and b, we find that for the 2DISC image without stitching, the false alarm rate is 0.4% for amplitude and 3% for phase at 90% detection probability; while for the full 2DISC panoramic amplitude and phase images, there is 100% detection without any false alarms.

especially when the sample is translated a small step, we can remove this noise by using the first order difference, which is defined as: $F_{n+1}(x,y) - F_n(x,y)$, where $F_n(x,y)$ denotes the nth phase or amplitude frame of the scan. However, it was found that the second order difference yields better noise reduction and image contrast. See the Supporting Information for a systematic study of the difference order. The second order difference image frame n is obtained as

$$F_{n+1}(x, y) - 2F_n(x, y) + F_{n-1}(x, y) \quad (1)$$

Figure 3 shows three different second order difference amplitude frames in an example array, the location of the defect is marked by the red rectangular box. In those images, the shift-invariant noise is removed, but due to time-variant noise, we still cannot clearly detect the 20 nm by 160 nm defect. Averaging in time of the images is a simple way to remove time-variant noise. However, instead of measuring for a long period of time at a single location, we translate the wafer and measure the defect at different locations in the image. Due to the large overlap of the adjacent frames, we obtain equivalent time-averaging (see Supporting Information) by stitching together all of the scan images to produce a panoramic average image. Translation and stitching with averaging further reduces system nonuniformity noise because the defect is measured at many different locations in the laser illumination and on the camera.

Figure 3d is the panoramic amplitude image of the example array. Similarly, Figure 3e is the panoramic phase image. Phase and amplitude images give different information about the defect. In Figure 3, parts d and e, the defect at the center can be clearly identified. However, the signal from the underlying structure reduces detectability. This signal can be complicated depending on the structure. Thus, if we want to extract just the defect information that is buried in the structure, we need to develop a suitable extraction algorithm.

After the second order difference and image stitching steps, the defect will appear as a tripole pattern of +1 −2 +1 (see Supporting Information for a schematic illustration). To detect this pattern, we convolve the final panoramic image with a matched tripole pattern. The matched tripole pattern $M(x,y)$ has a form of

$$M(x, y) = T(x + s, y) - 2T(x, y) + T(x - s, y) \quad (2)$$

where $T(x,y)$ is a test function and $s = 0.75$ μm is the translational step size. $T(x,y)$ should be optimized to obtain the maximum defect signal and reject the underlying structure. We designed $T(x,y)$ as a Gaussian function. Convolution serves as a low pass filter. We picked the standard deviation of the Gaussian to be 360 nm. This choice is large enough to filter out high frequency components in the second difference image due to the wafer's underlying structure, but small enough that it does not filter out the tripole pattern of the defect signal that has spacing $s = 0.75$ μm. See Supporting Information for a detailed discussion. In the end, we obtain a defect pattern matched panoramic image, i.e., the 2DISC image. Parts f and g of Figure 3 are the 2DISC amplitude and phase images of the example array, respectively. In both images, we can see the defect signal contrast has significantly improved as compared with Figure 3, parts d and e. For a quantitative study, we can compute the peak-signal-to-noise ratio (PSNR) (see Supporting Information). For the amplitude image, the PSNR increased by 7.0 dB from Figure 3d to Figure 3f. For the phase image, the PSNR increased by 8.7 dB from Figure 3e to Figure 3g. The 2DISC amplitude image in Figure 3f has slightly larger PSNR (1.8 dB) than the 2DISC phase image in Figure 3g. To validate that the overall approach of the 2DISC method with 0.75 μm step size is a good choice, we present a systematic study of PSNR for difference orders from zeroth to fourth order in the Supporting Information section. The study also examines the noise reductions from adding the image stitching step and the convolution step as well as the effects of changing the step size and the test function width.

The PSNR is a single number that can be useful to quickly evaluate the defect detection method. However, to study the improvement in defect detectability, ROC curves[41] are used since they quantify the trade-off between sensitivity and specificity of the defect classifier algorithm. Here, we will continue to discuss the previous 20 nm by 160 nm defect example. We first study how well we can find a defect in any single image frame. For the original image frames, we partition each frame into 4 μm by 4 μm submatrices, and then calculate |max − min| for each submatrix. Next, we classify the submatrix as defect containing if this difference is above a threshold. By varying the threshold, we generate an ROC curve. The blue curves in Figure 4, parts a and b, are the ROC curves for original amplitude and phase single frame images, respectively. On each figure, a random guess line is also plotted (black curve). The original image frames are similar to random guessing or sometimes even worse, possibly because the defect reduces the |max − min| variation from the underlying pattern. For comparison, we calculate the ROC for the second order

dx.doi.org/10.1021/nl401622b | Nano Lett. 2013, 13, 3716−3721

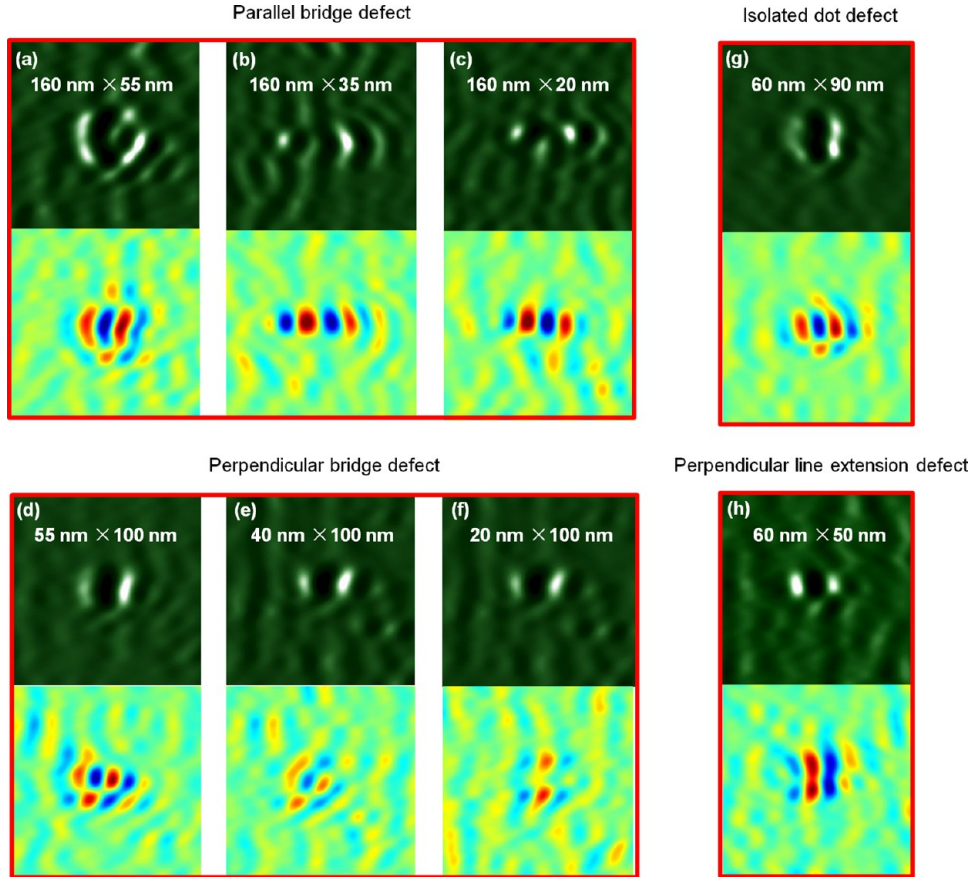

Figure 5. Defect detection results for different defect types using the 2DISC method. Each subfigure shows a 9 μm by 9 μm zoomed-in FOV phase image (top) and amplitude image (bottom). (a–c) Parallel bridge defects that are 160 nm by 55 nm, 160 nm by 35 nm, and 160 nm by 20 nm, respectively. (d–f) Perpendicular bridge defects that are 55 nm by 100 nm, 40 nm by 100 nm, and 20 nm by 100 nm, respectively. (g) Isolated dot defect that is 60 nm by 90 nm. (h) Perpendicular line extension defect that is 60 nm by 50 nm.

difference images with tripole convolution (2DC). These are shown in Figure 4, a and b, as red curves. Both curves are now well above the random guessing line. We achieve 90% detection probability with a false alarm rate of 0.4% for the amplitude image and 3% for the phase image. The lower false alarm rate for the amplitude image is attributed to the difference in the way the image postprocessing reduces additive and multiplicative noise and to the difference in the sensitivity of amplitude and phase to these types of noises. Finally, we studied the defect detection using the full 2DISC panoramic images; see the green curves in Figure 4, a and b. As expected (refer to Figure 3, f and g), we achieved 100% detection with no false alarms, which means we are able to accurately find the defect in the 70 μm by 27 μm panoramic image.

The same technique used to generate Figure 3, parts f and g, is also used for detection of other types of defects. For each 2DISC image, we show just a zoomed-in FOV (9 μm by 9 μm) around the defect in Figure 5. The phase image is on the top of each subfigure and the amplitude is on the bottom. For parallel bridge defects, we detected defects with sizes of 160 nm by 55 nm (Figure 5a), 160 nm by 35 nm (Figure 5b), and 160 nm by 20 nm (Figure 5c). For perpendicular bridge defects, we detected defects with sizes of 55 nm by 100 nm (Figure 5d), 40 nm by 100 nm (Figure 5e), and 20 nm by 100 nm (Figure 5f). We have detected 60 nm by 90 nm isolated dot defects (Figure 5g) and 60 nm by 50 nm perpendicular line extension defects (Figure 5h). The existence and locations of all these detected defects were confirmed by SEM (see Supporting Information). Note that, for the perpendicular bridge and line extension defects, the incident linear polarization was rotated parallel to the defect, i.e., perpendicular to the lines in the underlying structure. This maximizes the defect signal and minimizes the signal from the underlying structure. For all other types of defects, the polarization was parallel to the lines. In this way, we achieve the best detection for each type of defect.

In summary, we developed a nondestructive defect inspection method with large FOV using epi-DPM for image data collection and 2DISC for image postprocessing. Epi-DPM is a common-path interferometer which is insensitive to mechanical vibration noise. The measured interferograms from epi-DPM are used to retrieve the phase and amplitude images from the sample. Using the 2DISC method, panoramic phase and amplitude defect detection images are created, where significant defect signal contrast is achieved. The defect detectability is studied using ROC curves. This inspection method has successfully detected different types of defects with sizes down to 20 nm by 100 nm due to significant suppression of noise. To detect even smaller defects, laser power stabilization and system installation in a cleanroom environment should be implemented. This laser interferometry inspection method promises to advance many fields of nanotechnology research and development.

dx.doi.org/10.1021/nl401622b | *Nano Lett.* 2013, 13, 3716–3721

■ ASSOCIATED CONTENT

Supporting Information

Description of the phase and amplitude image retrieval theory and algorithms, a rigorous description of image postprocessing for defect signal extraction, and the SEM verification of the defect detection. This material is available free of charge via the Internet at http://pubs.acs.org.

■ AUTHOR INFORMATION

Corresponding Author

*(L.L.G.) E-mail: lgoddard@illinois.edu.

Author Contributions

R. Z., L.G., and G.P. conceived and designed the experiments. R. Z. and C. E. performed the DPM experiments. C.E., A. A., and R. Z. wrote the phase and amplitude retrieval programs. R. Z. and L.G. developed the image postprocessing methods. A. A. and R. Z. performed the SEM measurements. All authors interpreted the data, discussed the results, and wrote the paper.

Notes

The authors declare the following competing financial interest(s): G. P. is founder of Phi Optics, Inc., a company developing quantitative phase imaging technology for materials and life science applications.

■ ACKNOWLEDGMENTS

This research was funded by the Semiconductor Research Corporation (contract P13117). The work used instrumentation being developed with support from the National Science Foundation (NSF grant CBET-1040462 MRI) and matching funds from the University of Illinois. The authors express their gratitude to SEMATECH for providing the large area nanopatterned wafer.

■ REFERENCES

(1) Huang, J. S.; Callegari, V.; Geisler, P.; Bruning, C.; Kern, J.; Prangsma, J. C.; Wu, X. F.; Feichtner, T.; Ziegler, J.; Weinmann, P.; Kamp, M.; Forchel, A.; Biagioni, P.; Sennhauser, U.; Hecht, B. *Nature Commun.* **2010**, *1*, 150.

(2) Kalbac, M.; Hsieh, Y. P.; Farhat, H.; Kavan, L.; Hofmann, M.; Kong, J.; Dresselhaus, M. S. *Nano Lett.* **2010**, *10* (11), 4619−4626.

(3) Urita, K.; Sato, Y.; Suenaga, K.; Gloter, A.; Hashimoto, A.; Ishida, M.; Shimada, T.; Shinohara, H.; Iijima, S. *Nano Lett* **2004**, *4* (12), 2451−2454.

(4) Freer, E. M.; Grachev, O.; Duan, X. F.; Martin, S.; Stumbo, D. P. *Nature Nanotechnol.* **2010**, *5* (7), 525−530.

(5) Caironi, M.; Gili, E.; Sakanoue, T.; Cheng, X. Y.; Sirringhaus, H. *ACS Nano* **2010**, *4* (3), 1451−1456.

(6) Yang, H.; Heo, J.; Park, S.; Song, H. J.; Seo, D. H.; Byun, K. E.; Kim, P.; Yoo, I.; Chung, H. J.; Kim, K. *Science* **2012**, *336* (6085), 1140−1143.

(7) Goldstein, J. *Scanning electron microscopy and x-ray microanalysis*, 3rd ed.; Kluwer Academic/Plenum Publishers: New York, 2003.

(8) Leamy, H. J. *J. Appl. Phys.* **1982**, *53* (6), R51−R80.

(9) Rugar, D.; Hansma, P. *Phys. Today* **1990**, *43* (10), 23−30.

(10) Nguyen, C. V.; Stevens, R. M. D.; Barber, J.; Han, J.; Meyyappan, M.; Sanchez, M. I.; Larson, C.; Hinsberg, W. D. *Appl. Phys. Lett.* **2002**, *81* (5), 901−903.

(11) Kudo, T.; Bae, J.-B.; Dammel, R. R.; Kim, W.-K.; McKenzie, D. S.; Rahman, M. D.; Padmanaban, M.; Ng, W. *SPIE Proc.* **2001**, *4345*, 179−189.

(12) Egerton, R. F.; Li, P.; Malac, M. *Micron* **2004**, *35* (6), 399−409.

(13) Picco, L. M.; Bozec, L.; Ulcinas, A.; Engledew, D. J.; Antognozzi, M.; Horton, M. A.; Miles, M. J. *Nanotechnology* **2007**, *18* (4), 044030.

(14) Butt, H. J.; Siedle, P.; Seifert, K.; Fendler, K.; Seeger, T.; Bamberg, E.; Weisenhorn, A. L.; Goldie, K.; Engel, A. *J Microsc.-Oxford* **1993**, *169*, 75−84.

(15) Giessibl, F. J. *Rev. Mod. Phys.* **2003**, *75* (3), 949−983.

(16) Abbe, E. *J. R. Microsc. Soc.* **1881**, *1* (3), 388−423.

(17) Sandberg, R. L.; Song, C. Y.; Wachulak, P. W.; Raymondson, D. A.; Paul, A.; Amirbekian, B.; Lee, E.; Sakdinawat, A. E.; La-O-Vorakiat, C.; Marconi, M. C.; Menoni, C. S.; Murnane, M. M.; Rocca, J. J.; Kapteyn, H. C.; Miao, J. W. *Proc. Natl. Acad. Sci. U.S.A.* **2008**, *105* (1), 24−27.

(18) Seaberg, M. D.; Adams, D. E.; Townsend, E. L.; Raymondson, D. A.; Schlotter, W. F.; Liu, Y. W.; Menoni, C. S.; Rong, L.; Chen, C. C.; Miao, J. W.; Kapteyn, H. C.; Murnane, M. M. *Optics Express* **2011**, *19* (23), 22470−22479.

(19) Gardner, D. F.; Zhang, B. S.; Seaberg, M. D.; Martin, L. S.; Adams, D. E.; Salmassi, F.; Gullikson, E.; Kapteyn, H.; Murnane, M. *Opt. Expr.* **2012**, *20* (17), 19050−19059.

(20) Barnes, B. M.; Sohn, Y.-J.; Goasmat, F.; Zhou, H.; Silver, R. M.; Arceo, A. *Proc. SPIE* **2012**, *8324*, 83240F.

(21) Wagner, C.; Harned, N. *Nat. Photonics* **2010**, *4* (1), 24−26.

(22) Liu, Z. H.; Goldberg, B. B.; Ippolito, S. B.; Vamivakas, A. N.; Unlu, M. S.; Mirin, R. *Appl. Phys. Lett.* **2005**, *87* (7), 071905 .

(23) Ippolito, S. B.; Goldberg, B. B.; Unlu, M. S. *Appl. Phys. Lett.* **2001**, *78* (26), 4071−4073.

(24) Serrels, K. A.; Ramsay, E.; Warburton, R. J.; Reid, D. T. *Nat. Photonics* **2008**, *2* (5), 311−314.

(25) Mansfield, S. M.; Kino, G. S. *Appl. Phys. Lett.* **1990**, *57* (24), 2615−2616.

(26) Mason, D. R.; Jouravlev, M. V.; Kim, K. S. *Opt. Lett.* **2010**, *35* (12), 2007−2009.

(27) Rosenfeld, A.; Lorenz, M.; Stoian, R.; Ashkenasi, D. *Appl. Phys. A: Mater.* **1999**, *69*, S373−S376.

(28) Papernov, S.; Schmid, A. W. *J. Appl. Phys.* **1997**, *82* (11), 5422−5432.

(29) Bonneau, F.; Combis, P.; Rullier, J. L.; Vierne, J.; Pellin, M.; Savina, M.; Broyer, M.; Cottancin, E.; Tuaillon, J.; Pellarin, M.; Gallais, L.; Natoli, J. V.; Perra, M.; Bercegol, H.; Lamaignere, L.; Loiseau, M.; Donohue, J. T. *Appl. Phys. B* **2002**, *75* (8), 803−815.

(30) Hellman, A. N.; Vahidi, B.; Kim, H. J.; Mismar, W.; Steward, O.; Jeon, N. L.; Venugopalan, V. *Lab Chip* **2010**, *10* (16), 2083−2092.

(31) Zheng, G. A.; Lee, S. A.; Antebi, Y.; Elowitz, M. B.; Yang, C. H. *Proc. Natl. Acad. Sci. U.S.A.* **2011**, *108* (41), 16889−16894.

(32) Min, W.; Freudiger, C. W.; Lu, S. J.; Xie, X. S. *Annu. Rev. Phys. Chem.* **2011**, *62*, 507−530.

(33) Mudanyali, O.; Mcleod, E.; Luo, W.; Greenbaum, A.; Coskun, A. F.; Hennequin, Y.; Allier, C. P.; Ozcan, A. *Nat. Photon.* **2013**, *7* (3), 240−247.

(34) Kner, P.; Chhun, B. B.; Griffis, E. R.; Winoto, L.; Gustafsson, M. G. L. *Nature Methods* **2009**, *6* (5), 339−U36.

(35) Wang, Z.; Millet, L.; Mir, M.; Ding, H. F.; Unarunotai, S.; Rogers, J.; Gillette, M. U.; Popescu, G. *Opt. Expr.* **2011**, *19* (2), 1016−1026.

(36) Popescu, G. *Quantitative Phase Imaging of Cells and Tissues*; McGraw-Hill: New York, 2011.

(37) Popescu, G.; Ikeda, T.; Dasari, R. R.; Feld, M. S. *Opt. Lett.* **2006**, *31* (6), 775−777.

(38) Park, Y.; Popescu, G.; Badizadegan, K.; Dasari, R. R.; Feld, M. S. *Opt. Lett.* **2007**, *32* (7), 811−813.

(39) Edwards, C.; Arbabi, A.; Popescu, G.; Goddard, L. L. *Light Sci. Appl.* **2012**, *1*, e30.

(40) Ikeda, T.; Popescu, G.; Dasari, R. R.; Feld, M. S. *Opt. Lett.* **2005**, *30* (10), 1165−1167.

(41) Zweig, M. H.; Campbell, G. *Clin. Chem.* **1993**, *39* (8), 1589−1589.